

Spin-coating on nanoscale topography and phase separation of diblock copolymers

Richard Farrell,
CRANN Industry representative

Jean P.F. Charpin¹, Vincent Cregan¹, James P. Gleeson¹, Michael Hayes²,
William Lee¹, Stephen B.G. O'Brien¹, Michael Vynnycky¹

¹*MACSI, Department of Mathematics & Statistics,
University of Limerick.*

²*School of Mathematics, Statistics and Applied Mathematics,
National University of Ireland, Galway.*

April 11, 2008

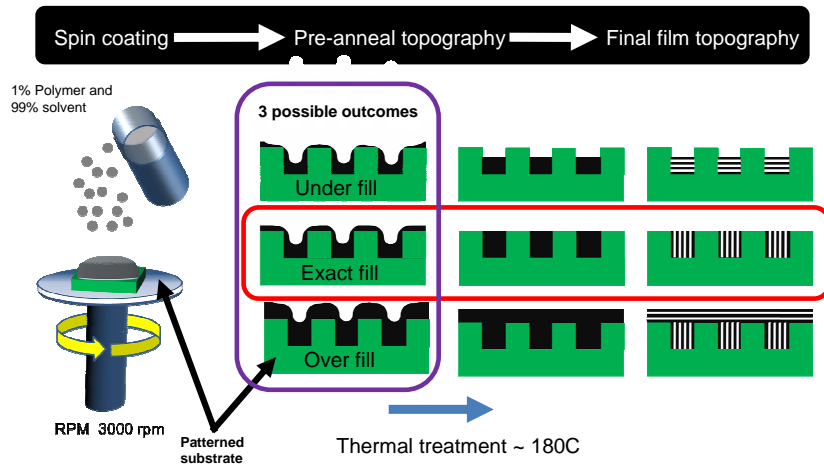


Figure 1: Summary of the process under study: spin-coating of polymer onto patterned substrates leads to a dry polymer profile; after annealing the polymer has flowed into trenches and phase-separates to create the desired patterns. Both under-fill and over-fill cases are undesirable, as the resulting nanostructures are not suitably patterned.

0.1 Introduction

Diblock copolymer thin films have attracted significant recent interest because of their potential applications in nanofabrication. Diblock copolymers are macromolecules consisting of two chemically distinct polymer chains covalently bonded together at one junction point. It is well-known that a molten collection of these molecules microphase-segregates below an order-disorder transition temperature to form a myriad of interesting nano/microstructures [1].

In the process under study at CRANN, various diblock copolymers are dissolved in solvent and spin-coated onto a patterned silicon wafer, see Figure 1. Several possible configurations for the trenches are employed, see Figures 2 and 3 for examples. Following the spin-coating the nanostructured films undergo a thermal anneal at approximately 200°C for up to 24 hours, and the polymer flows, phase-separates and self-assembles into well defined nanostructures with periodicities approaching 10 nm (right hand panel of Figure 1).

CRANN researchers are interested in mathematical modelling of all aspects of the process, with the aim of removing expensive trial and error design cycles. Of particular interest is the flow of the polymer during spin-coating, and also during the subsequent annealing process. This defines Problem 1:

- **Problem 1:** Describe how the spin-coating process is affected by the geometrical configuration of trenches (see side profiles in Figure 3). How should parameters be adjusted to optimize quality of trench-filling (so over-filling or under-filling are avoided or minimized)?

Also of considerable interest is the chemical process of phase-separation and self-assembly of the diblock

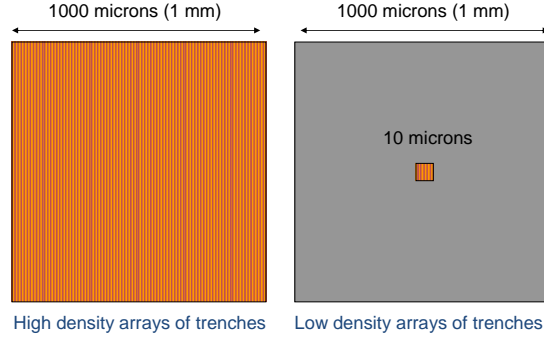


Figure 2: Schematic of possible trench arrangements and dimensions (top view).

copolymer. Existing models in the literature rely heavily on computationally expensive Monte-Carlo simulation methods. Problem 2 may be expressed as:

- **Problem 2:** Model the phase-separation process for the polymers, with a particular interest in how polymers self-organize in a corner geometry.

The modelling work performed during the study group is summarized in this report (and in a presentation to the CRANN researchers). The report is split into four main sections, with discussion and suggestions for experiments in the concluding section. The content of the sections is as follows:

- **Section 0.2:** Mathematical modelling of spin-coating onto a flat substrate; no annealing considered.
- **Section 0.3:** Modelling of spin-coating onto a substrate with topography (i.e. trenches); no annealing considered.
- **Section 0.4:** Flow of polymer during annealing.
- **Section 0.5:** Models for self-assembly of polymers into nanostructures.

Sections 0.2 to 0.4 are focussed on the fluid flow problems for the polymer, and go some way to providing useful answers to Problem 1. On the other hand, Problem 2 was found to be extremely challenging, and the efforts described in section 0.5 represent only a relatively modest impact on this problem.

0.2 Spin-coating onto flat substrates

Emslie, Bonner and Peck described the flow of a viscous Newtonian liquid on a rotating planar surface first [2]. In their model, only centrifugal and viscous forces are considered while surface tension, gravity and Coriolis forces are neglected. In addition, they assume that the radial expansion is large relative to the film thickness. Thus, lubrication theory is applicable. The centrifugal force balances the viscous forces

What is the effect on self-assembly when broad/narrow mesas/trenches are used? Design rules would be very useful...

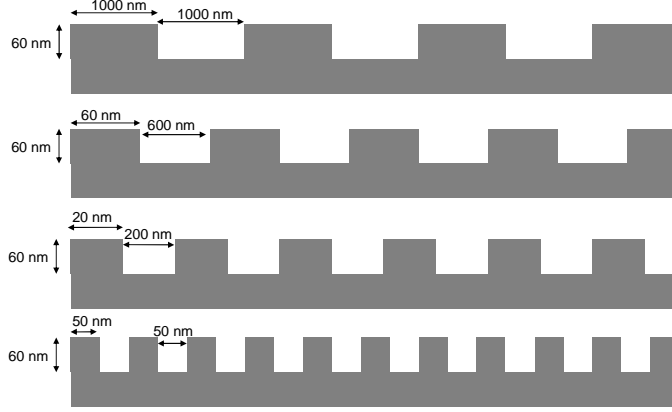


Figure 3: Schematic of possible trench arrangements and dimensions (side view).

and the solution of the resulting hydrodynamic equation is a uniform film independent of the initial fluid profile. This model is not sufficient for the present study since it only describes the behaviour of a fluid, it does not account for solvent evaporation which is ultimately responsible for the final solid film thickness.

Meyerhofer [3] was the first to acknowledge the importance of evaporation in the spin-coating model. The approach he developed allows for evaporation of the solvent at the end of process and this leads to a solid film similar to the phenomenon investigated in the present study. The solution is valid for Newtonian fluids and approximately Newtonian fluid/particle mixtures.

Meyerhofer assumed the process could be approximated by two sub-processes, each of them lasting for about the same amount of time.

1. Evaporation is neglected for the initial stage and the film thins via flow. This initial stage ends when evaporation balances the flow. This occurs at the time:

$$t_{1/2} = \left(\frac{1}{l_{1/2}^2} - \frac{1}{L_0^2} \right) \frac{3\mu}{4\rho\omega^2}, \quad (1)$$

where L_0 represents the initial solvent height, defined as the liquid thickness obtained by removing all the solute, $\omega/(2\pi)$ is the number of rotations per second, μ denotes the dynamic viscosity and ρ is the density. At $t_{1/2}$, the solvent height, $l_{1/2}$, and the solute height, defined as the liquid thickness obtained by removing all the solvent, $s_{1/2}$, are:

$$l_{1/2} = \left(\frac{3\mu E}{2\rho\omega^2} \right)^{1/3}, \quad s_{1/2} = \frac{S_0}{L_0} \left(\frac{3\mu E}{2\rho\omega^2} \right)^{1/3}, \quad (2)$$

where S_0 is the initial solute height and E denotes the evaporation rate.

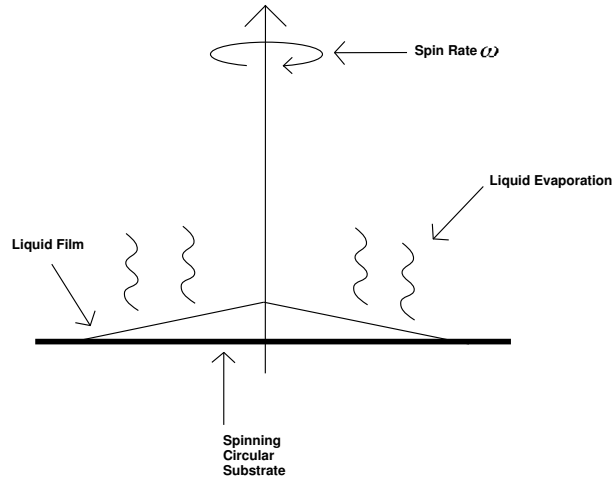


Figure 4: Spin-coating overview

2. During the final stage, the flow may be completely neglected and the film thins via evaporation. The process concludes at time $t = t_f$, when the solvent has been completely evaporated off. The remaining solute thickness, s_f , and the final time t_f may be calculated as:

$$t_f = \frac{1}{E} (l_{1/2} + Et_{1/2}) , \quad s_f = \frac{S_0}{L_0} \left(\frac{3\mu E}{2\rho\omega^2} \right)^{1/3} . \quad (3)$$

While Meyerhofer gives a good approximation for the final film thickness, his assumption about the length of the two sub-processes is incorrect: during most of the process, flow and evaporation have the same order of magnitude, see Figure 5. Flow only dominates for a short period at the start of the process and evaporation only becomes the leading order process at the very end when solute concentration is high. Cregan and O' Brien [4] used perturbation theory to evaluate the length of each stage. They show that the initial stage lasts for $\Delta t \sim (3\mu)/(2L_0^2\rho\omega^2)$. The flow dominates until the solvent thickness is:

$$L \sim \left(\frac{3\mu E}{2\rho\omega^2} \right)^{1/3} . \quad (4)$$

The second relatively long stage lasts for $\Delta t \sim [(3\mu)/(2\rho\omega^2 E^2)]^{1/3}$. Evaporation only dominates during a very short time interval at the end $\Delta t \sim (S_0/L_0)[(3\mu)/(2\rho\omega^2 E^2)]^{1/3}$.

The asymptotic solution for the final solute thickness is identical to Meyerhofer's solution. The drying time however differs from Equation (1) and becomes:

$$t_f^* = \frac{2\pi}{3\sqrt{3}} \left(\frac{3\mu}{2\rho\omega^2 E^2} \right)^{1/3} . \quad (5)$$

This drying time is 10% to 20% shorter than the value calculated using Meyerhofer value.

The results presented in this section will be used in future work validate numerical results.

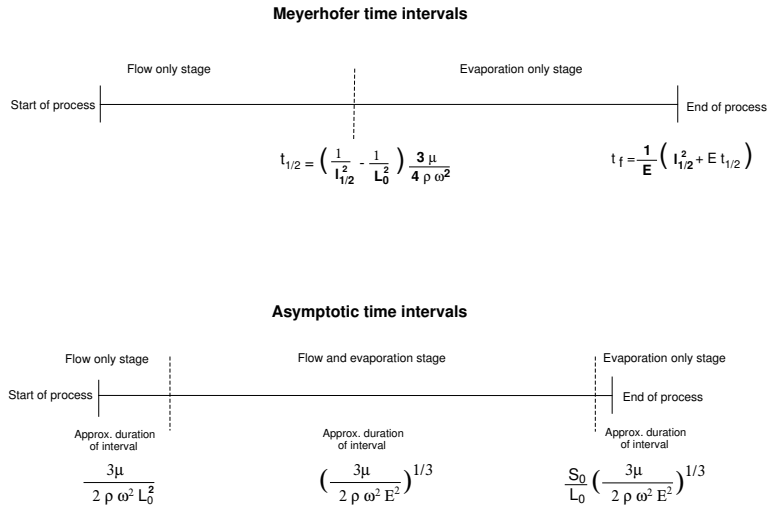


Figure 5: Time comparisons

0.3 Model for spin-coating with topography

A model for the thin film flow over topography is derived using lubrication theory. Two complementary approaches to solving this equation are pursued: in Section 0.3.2 we examine a perturbation method valid for small topography, while Section 0.3.3 gives the description and results of computational solutions of the full equation.

0.3.1 Thin-film flow over topography

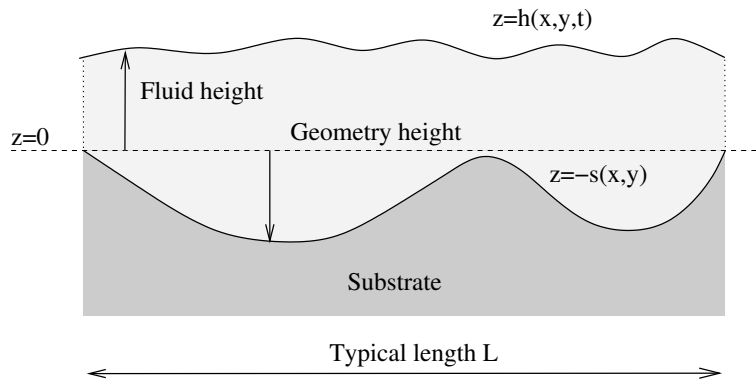


Figure 6: Definition of the typical geometry

The governing equation for the phenomenon will now be derived. A typical configuration is shown on

Figure 6. A thin fluid layer flows over an irregular substrate: the level $z = 0$ is defined by the highest point of the substrate and the fluid height above and below this reference level are denoted h and $-s$ respectively. As many problems in Computational Fluid Dynamics, the equations governing the fluid flow are based on the Navier Stokes and continuity equations. Since the typical fluid height, h_0 , is much smaller than the typical length L , there is no need to solve for the complete system, the Navier Stokes equations may be simplified using lubrication theory [5, 6]. This leads to the following equations for the components (u, v, w) of the velocity vector and the pressure p (see Nomenclature section for list of symbols):

$$\mu \frac{\partial^2 u}{\partial z^2} = \frac{\partial p}{\partial x} + \rho \omega^2 x + \mathcal{O}(\epsilon^2, \epsilon^2 Re) , \quad (6)$$

$$\mu \frac{\partial^2 v}{\partial z^2} = \frac{\partial p}{\partial y} + \rho \omega^2 y + \mathcal{O}(\epsilon^2, \epsilon^2 Re) , \quad (7)$$

$$\frac{\partial p}{\partial z} = -\rho g + \mathcal{O}(\epsilon^2, \epsilon^2 Re) , \quad (8)$$

$$0 = \frac{\partial u}{\partial x} + \frac{\partial v}{\partial y} + \frac{\partial w}{\partial z} , \quad (9)$$

where $\epsilon = h_0/L$ is the aspect ratio of the flow and $\epsilon^2 Re$ is the reduced Reynolds number. Both the density ρ and the dynamic viscosity μ vary linearly with the composition of the fluid:

$$\mu = \mu_0(1 - c) + \mu_1 c , \quad \rho = \rho_0(1 - c) + \rho_1 c ,$$

and the quantities with the subscripts 0 and 1 denote the values for solvent and polymer respectively. The governing equations may be non-dimensionalised using the following scales:

$$\begin{aligned} x = Lx' , \quad y = Ly' , \quad z = h_0 z' = \epsilon Lz' , \quad \mu = \mu_0 \mu' , \quad \rho = \rho_0 \rho' , \quad u = Uu' = \frac{\epsilon^2 L^3 \rho \omega^2}{3\mu_0} u' , \\ v = Uv' , \quad w = \epsilon U w' , \quad t = \tau t' = \frac{L}{U} t' , \quad p = Pp' = \frac{3\mu_0 U}{\epsilon^2 L} p' = L^2 \rho \omega^2 p' , \quad E = \epsilon U E' = \frac{h_0^3 \rho \omega^2 E'}{3\mu_0} . \end{aligned}$$

The pressure scale, P , is standard for lubrication theory. The velocity scale, U , is determined by the driving force of the flow, the centrifugal force $\rho \omega^2(x, y)$. The length scale, L , and the height scale, h_0 , impose the velocity scale in the z direction, ϵU . The evaporation scale leads to the standard wetting scale. This leads to the wetting height:

$$h_w = \left(\frac{3\mu_0 E}{\rho \omega^2} \right)^{1/3} . \quad (10)$$

This height differs from the Meyerhofer value by a factor $^3\sqrt{2}$. This modification leads to a simpler governing equation but does not fundamentally change the results. Using the scaled parameters and dropping the primes immediately, these governing equations become:

$$\mu \frac{\partial^2 u}{\partial z^2} = 3 \frac{\partial p}{\partial x} + 3\rho x + \mathcal{O}(\epsilon^2, \epsilon^2 Re) , \quad (11)$$

$$\mu \frac{\partial^2 v}{\partial z^2} = 3 \frac{\partial p}{\partial y} + 3\rho y + \mathcal{O}(\epsilon^2, \epsilon^2 Re) , \quad (12)$$

$$\frac{\partial p}{\partial z} = -\rho \beta + \mathcal{O}(\epsilon^2, \epsilon^2 Re) , \quad (13)$$

$$0 = \frac{\partial u}{\partial x} + \frac{\partial v}{\partial y} + \frac{\partial w}{\partial z} , \quad (14)$$

where

$$\beta = \frac{\epsilon^3 \rho_0 g L^2}{3\mu_0 U} = \frac{\epsilon g}{L \omega^2} .$$

The equations are solved using the following boundary conditions:

- No slip at the fluid-substrate interface:

$$u(-s) = v(-s) = w(-s) = 0 ,$$

- No shear stress at the air-fluid interface:

$$\mu \frac{\partial u}{\partial x} \Big|_{z=h} = \mu \frac{\partial v}{\partial y} \Big|_{z=h} = 0 ,$$

- Pressure jump at the air-fluid interface:

$$p(h) = p_0 - \alpha \nabla^2 h = p_0 - \frac{\epsilon^3 \sigma}{3\mu U} \nabla^2 h = p_0 - \frac{\epsilon \sigma}{\rho \omega^2 L^3} \nabla^2 h ,$$

- The standard kinematic condition, including the evaporation term, is also applied at the free surface:

$$w(h) = \frac{\partial h}{\partial t} + u \frac{\partial h}{\partial x} + v \frac{\partial h}{\partial y} + E .$$

A straightforward integration of Equations (11–13) provides expressions for the pressure and velocities. Integrating the continuity equation (14) across the fluid layer with respect to the kinematic condition leads to the mass balance:

$$\frac{\partial h}{\partial t} + \frac{\partial}{\partial x} \left(\int_{-s}^h u dz \right) + \frac{\partial}{\partial y} \left(\int_{-s}^h v dz \right) = \frac{\partial h}{\partial t} + \frac{\partial Q^x}{\partial x} + \frac{\partial Q^y}{\partial y} = -E . \quad (15)$$

where Q^x and Q^y denote the fluxes in the x and y directions respectively,

$$\begin{aligned} Q^x &= (h+s)^3 \left[\frac{\alpha}{\mu} \left(\frac{\partial^3 h}{\partial x^3} + \frac{\partial^3 h}{\partial x \partial y^2} \right) - \frac{\beta \rho}{\mu} \frac{\partial h}{\partial x} + \frac{\rho x}{\mu} \right] \\ Q^y &= (h+s)^3 \left[\frac{\alpha}{\mu} \left(\frac{\partial^3 h}{\partial x^2 \partial y} + \frac{\partial^3 h}{\partial y^3} \right) - \frac{\beta \rho}{\mu} \frac{\partial h}{\partial y} + \frac{\rho y}{\mu} \right] \end{aligned}$$

The governing equation (15) may then be written as:

$$\frac{\partial h}{\partial t} + \nabla \cdot \left[\frac{(h+s)^3}{\mu} (\alpha \nabla (\nabla^2 h) - \beta \rho \nabla h) \right] + \nabla \cdot \left(\frac{\rho r (h+s)^3}{\mu} \mathbf{e}_r \right) = -E. \quad (16)$$

If the density and viscosity are constant, this equation becomes:

$$\frac{\partial h}{\partial t} + \nabla \cdot [(h+s)^3 (\alpha \nabla (\nabla^2 h) - \beta \rho \nabla h)] + \nabla \cdot (r(h+s)^3 \mathbf{e}_r) = -E. \quad (17)$$

These governing equations are typical for thin film flows over a surface with a varying topography. The steady-state version of Equation (17) is derived for a gravity driven flow over topography in [7]. Time dependent versions of (17) is found for a general driving force in [8] and in the spin coating context in [9]. The gravity driven version of (16) over a flat surface may be found in [10]. In the present study, the standard Equation (16) governing fluid height is coupled with another equation governing the solute concentration c . This equation is a straightforward extension of Equation (16):

$$\frac{\partial (ch)}{\partial t} + \nabla \cdot (c\mathbf{Q}) = 0 \quad (18)$$

where $\mathbf{Q} = (Q_x, Q_y)$ are the the fluxes defined above.

The model is now complete and the equations will be solved, first using a perturbation method and then numerically.

0.3.2 Perturbation approach

If the surface topography is small compared to the fluid thickness, the film height h is dominated by a spatially-independent term $h_0(t)$, and the first order perturbation term $h_1(x, y)$ is time independent. We may seek a solution of Equation (17) in the form of a regular perturbation series:

$$h(\mathbf{x}, \mathbf{y}, t) = h_0(t) + \delta h_1(\mathbf{x}, \mathbf{y}) + \dots \quad (19)$$

The small parameter δ represents the size of the topography scale compared to the spatially-independent film height $h_0(t)$. At the end of the process $h_0 = 0$ and the first order perturbation h_1 and its spatial derivatives vanish at infinity. The first term in the corresponding series for the topography s is therefore of order δ :

$$s(\mathbf{x}) = \delta s_1(\mathbf{x}) + \dots \quad (20)$$

Combining Equations (17) and (19) provides the leading order film height equation:

$$\frac{dh_0}{dt} = -2h_0^3 - 1. \quad (21)$$

The corresponding first order film height equation is:

$$6(h_1 + s_1) + 3 \left[x \frac{\partial(h_1 + s_1)}{\partial x} + y \frac{\partial(h_1 + s_1)}{\partial y} \right] + \alpha h_0 \left[\frac{\partial^4 h_1}{\partial x^4} + 2 \frac{\partial^4 h_1}{\partial x^2 \partial y^2} + \frac{\partial^4 h_1}{\partial y^4} \right] - \beta h_0 \left[\frac{\partial^2 h_1}{\partial x^2} + \frac{\partial^2 h_1}{\partial y^2} \right] = 0. \quad (22)$$

To check the consistency between the perturbation method and the numerical method, we will compute the first order scaled fluid thickness h_1 with some simplifications using the Green function method, see Appendix .1.

- The last term in (22) is neglected because it results from pressure due to fluid thickness which is negligible in comparison to the centrifugal effect.
- The first term which does not include derivatives is also neglected as it is much smaller than the other terms - this can be easily seen a posteriori.
- We will look at radially symmetric topographies. To approximately solve for h_1 with these topographies, we will temporally change to polar coordinates and define r to be the scaled radial distance from the centre of rotation.

Making the coordinate change and assuming we are looking for a solution in the region of $r = 1$, Equation (22) simplifies to:

$$(\alpha h_0/3) \frac{d^3 h_1(r)}{dr^3} + h_1(r) = -s_1. \quad (23)$$

The Green function g associated with (23) satisfies the equation:

$$(\alpha h_0/3) \frac{d^3 g(r - r_0)}{dr^3} + g(r - r_0) = \delta(r - r_0). \quad (24)$$

The Green function may then be written as:

$$g(r - r_0) = \begin{cases} \frac{2}{3} \left(\frac{3}{\alpha h_0} \right)^{1/3} \exp \left[\frac{1}{2} \left(\frac{3}{\alpha h_0} \right)^{1/3} (r - r_0) \right] \cos \left[\frac{\sqrt{3}}{2} \left(\frac{3}{\alpha h_0} \right)^{1/3} (r - r_0) + \frac{\pi}{3} \right] & r < r_0 \\ \frac{1}{3} \left(\frac{3}{\alpha h_0} \right)^{1/3} \exp \left[- \left(\frac{3}{\alpha h_0} \right)^{1/3} (r - r_0) \right] & r > r_0. \end{cases} \quad (25)$$

Using the Green function, the first order perturbation may be expressed as:

$$h_1(r) = - \int_{-\infty}^{\infty} s_1(r_0)g(r-r_0)dr_0. \quad (26)$$

In most cases, the integral in Equation (26) may only be calculated numerically or lead to rather complex expressions. A simple analytical solution may however be found for a step of one unit at $r = 1$ (δH in dimensional units)

$$s_1(r) = \begin{cases} 1 & r < 1 \\ 0 & r > 1. \end{cases} \quad (27)$$

Inserting this into Equation (26) leads to

$$h_1(r) = \begin{cases} \frac{2}{3} \exp \left[\frac{1}{2} \left(\frac{3}{\alpha h_0} \right)^{1/3} (r-1) \right] \cos \left[\frac{\sqrt{3}}{2} \left(\frac{3}{\alpha h_0} \right)^{1/3} (r-1) \right] - 1 & r < 1 \\ -\frac{1}{3} \exp \left[- \left(\frac{3}{\alpha h_0} \right)^{1/3} (r-1) \right] & r > 1. \end{cases} \quad (28)$$

This curve may be seen on Figure 7. As could be expected, the fluid surface is mainly perturbed for $0.7 \leq r \leq 1.1$ and a hump typical of thin films with high surface tension forms before the step. Very quickly, the fluid height on either side is constant with its value imposed by the underlying topography, $h_1 = -1$ to the left of the step and $h_1 = 0$ to the right.

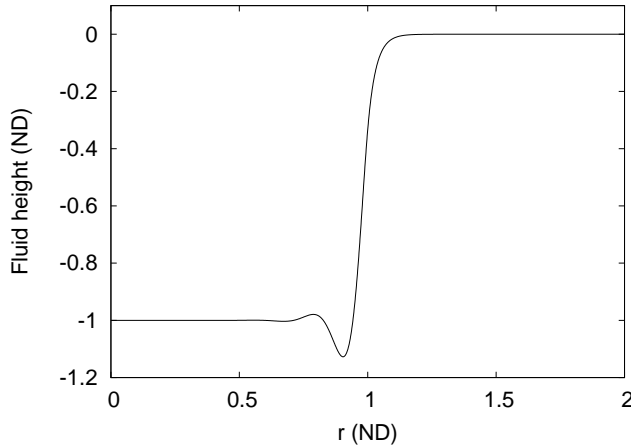


Figure 7: First order perturbation for a step at $r = 1$

The topography described here leads to an analytical solution. There is no simple analytical solution for all the other cases studied in the report. In the following, when using the Green function method, the integral (26) will be evaluated numerically. However, according to the values of the Green function, the perturbation should extend over a length similar to that seen in Figure 7 even for the series of small trenches considered in the following sections.

The solution provided by this method is not valid all the time, it describes a radially symmetric geometry. When considering the typical cases suggested by CRANN, comparison may only be performed at specific locations, as will be performed in the following.

0.3.3 Numerical solution of full equations

The system will now be solved numerically over the surface $[x_{min}; x_{max}][y_{min}; y_{max}]$, using a standard numerical method. The system rotates around $(0,0)$. The fluid height, h , and the concentration, c , are calculated on equally spaced points numbered from 0 to n_x and 0 to n_y , including the boundaries, separated by the space steps Δx and Δy . The simulation time t_m is divided in n_t time steps denoted $\Delta t = t_m/n_t$. The fluid height and concentration at $x = x_{min} + i\Delta x$, $y = y_{min} + j\Delta y$ and $t = k\Delta t$ are denoted $h_{i,j}^k$ and $c_{i,j}^k$ respectively.

Numerical scheme

A typical numerical scheme in conservative form for the governing Equations (17) and (18) may be written:

$$h_{i,j}^{k+1} = h_{i,j}^k - \frac{\Delta t}{\Delta x} \left(Q_{i+1/2,j}^x - Q_{i-1/2,j}^x \right) - \frac{\Delta t}{\Delta y} \left(Q_{i,j+1/2}^y - Q_{i,j-1/2}^y \right) - E\Delta t, \quad (29)$$

$$c_{i,j}^{k+1} = \frac{1}{h_{i,j}^{k+1}} \left[c_{i,j}^k h_{i,j}^k - \frac{\Delta t}{\Delta x} \left(c_{i+1/2,j}^k Q_{i+1/2,j}^x - c_{i-1/2,j}^k Q_{i-1/2,j}^x \right) - \frac{\Delta t}{\Delta y} \left(c_{i,j+1/2}^k Q_{i,j+1/2}^y - c_{i,j-1/2}^k Q_{i,j-1/2}^y \right) \right], \quad (30)$$

where $W_{i+1/2,j}$ represents the value of W at $x = x_{min} + (i + 1/2)\Delta x$, $y = y_{min} + j\Delta y$.

Since the fluxes are non linear, calculating all terms implicitly is not possible. An alternative is presented in [11] for a one dimensional domain: the derivatives of the film height are evaluated at time $t = (k + 1)\Delta t$ and all the other terms are calculated explicitly at time $t = k\Delta t$. Solving for the fluid height at time $(k + 1)\Delta t$ requires the inversion of a penta-diagonal matrix that may be performed easily using a LU algorithm. The generalization to a two dimensional space would require the inversion of a broadly banded matrix. An alternative method is to replace the semi implicit scheme by an Alternative Direction Implicit (ADI) scheme, or Peaceman-Rachford non-homogeneous scheme [12, 13]. The time step is then divided into two equal parts: when $t \in [k, k + 1/2]\Delta t$ the flux is evaluated implicitly in the x direction and explicitly in the y direction; during $t \in [k + 1/2, k + 1]\Delta t$ the flux is evaluated explicitly in the x direction and implicitly in the y direction. The cross derivatives terms could be calculated implicitly but they would add non penta-diagonal terms to the matrix. If the cross terms are evaluated explicitly, the film height may be determined by inverting two penta-diagonal matrices during each time step.

Results with constant concentration

The fluid layer will now be simulated with a constant concentration using the values detailed in the Nomenclature section. For the aspect ratio $\epsilon = 0.0025$, the wetting height and the non-dimensional parameters may be estimated as

$$h_w = 3.72 \cdot 10^{-6} m, \quad \alpha = 2 \cdot 10^{-4}, \quad \beta = 1.5 \cdot 10^{-4}.$$

The parameters α and β are nearly equal. The first order derivative of the height being generally of significantly lower magnitude than the third order derivative, this leads to

$$|\beta \nabla h| \ll |\alpha \nabla (\nabla^2 h)|.$$

Consequently, the gravity term $|\beta \nabla h|$ may be neglected in the governing equation. The following simulations are performed over a surface. However, for practical reasons, all of the curves presented here are cross sections: this makes comparisons between the various results much easier.

The evolution of the fluid layer is first studied over a single infinitely long trench of depth 0.02 and located between $1 \leq x \leq 1.5$. At $t = 0$, the fluid layer is initialised at 100 times the wetting height. The

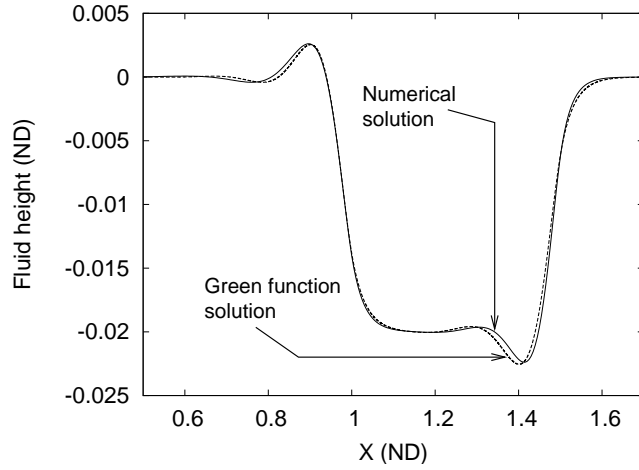


Figure 8: Fluid surface shape over the trench

trench affects the surface of the fluid right from the start. Very quickly, two humps appear on either side of the trench, due to the effects of surface tension and higher fluid velocity in the trench as may be seen on Figure 8. This shape remains approximately constant over time but remains small compared to the average height over the surface during most of the simulation. This solution may be compared around $y \sim 0$ with the radially symmetric solution calculated using the Green function. The first order perturbations calculated with both methods compare well as may be seen on Figure 8 and this validates the numerical scheme.

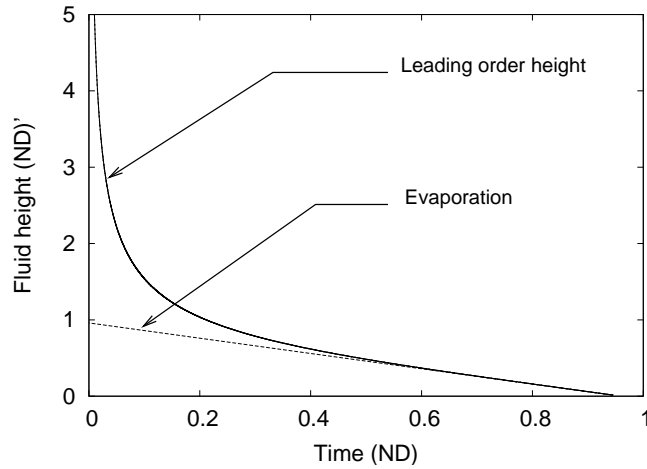


Figure 9: Evolution of the height over the surface

Except for the small oscillations above the trench, the fluid layer is flat. The evolution of the height is shown in Figure 9. The fluid height is compared with the amount of fluid evaporated and a comparison with the analytical results calculated using Equation (21). The numerical and analytical curves are

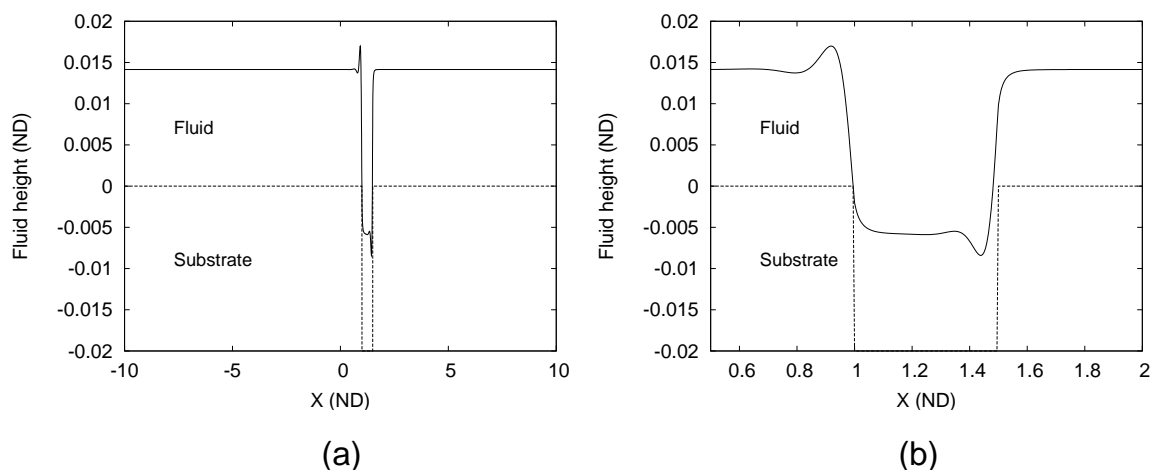


Figure 10: Final fluid shape over the trench

indistinguishable for the entire simulation. This again validates the numerical scheme developed. The curve labelled ‘evaporation’ shows the amount of fluid evaporated during the process. At the start of the simulation, until $t \sim 0.01$. Flow and evaporation are of similar order of magnitude for $0.01 \leq t \leq 0.4$ and evaporation dominates afterwards. This description does not really fit with the model developed by Meyerhofer [3] but is consistent with the study conducted by Cregan and O’Brien [4] but the times they calculate may not be compared since they consider a fluid solute mixture.

Figure 10 shows the fluid layer at the end of the simulation. At this stage, fluid disappears from the surface. The complete layer is shown on Figure 10a and a close up around the trench is shown on Figure 10b. The fluid thickness has not been significantly affected over the entire simulation. This could however change if the simulation was extended. However, the process is no longer realistic at this stage: in practice, the polymer dissolved in the fluid may not evaporate and a minimum height of fluid should always remain. The complete equation (16) coupled with the concentration equation (18) will prevent this inconsistency. This will not be performed in this report. However, the final polymer height could be approximated by the product of height and initial concentration when the wetting height is reached away from the perturbation.

The fluid height is now studied for a set of trenches shown on Figure 11: the distances are non-dimensionalised but they correspond to 240nm wide trenches separated by 240nm and 60nm deep. These topography variations are only located around $x = 1$ but the oscillation created on the fluid surface is considerably wider—compare the horizontal scales of Figure 11 and Figure 12. This perturbation is the same order of magnitude as the perturbation created with the previous geometry. Here again, the numerical solution compares extremely well with the analytical solution calculated using the Green function of Equation (26).

Finally, Figures 13 and 14 show the fluid layer at the end of the simulation when the fluid disappears. The layer becomes zero ahead of the trenches. The oscillations above the trenches, see Figure 13b, are present during the entire simulation but may only be noticed when the fluid layer is extremely thin because of their very small amplitude. However, as already mentioned, the model may no longer be valid at this point and the concentration equation (18) must also be solved numerically. This will be investigated in a further study.

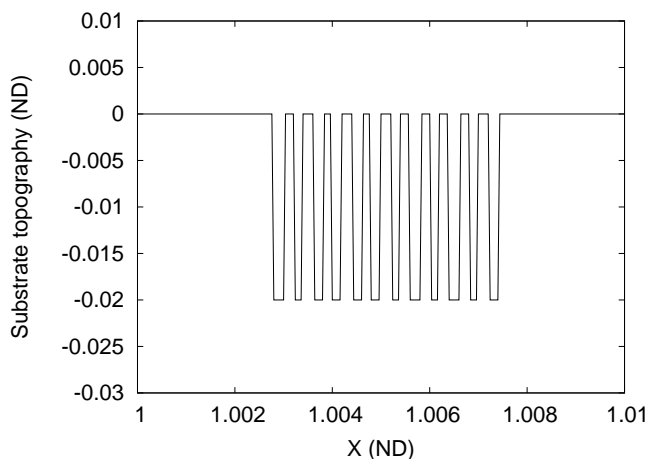


Figure 11: Geometry of the trenches

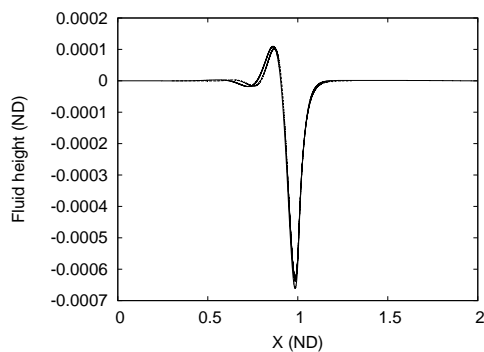


Figure 12: Fluid surface shape over the set of trenches

0.4 Flow during annealing

It is clear from the results of section 0.3 that the detailed profile of the polymer following spin-coating onto a surface with topography (but before annealing) is rather complicated. One of the challenges posed by CRANN researchers is to find a set of design rules for high-density mesa/trench configurations (with spin-coating parameters) which lead to perfect filling of trenches. In this section we therefore assume that the dry polymer is simply conformal with the topography (i.e. the same height of polymer is deposited on all mesas and into all trenches). In light of the results of section 0.3 this may be a rather crude approximation, as the local variations in polymer height (as depicted in Figure 12, say) may be up to approximately 10% of the total height. Nevertheless, it is possible to derive some simple design rules using this assumption, and we can directly compare with experimental results.

We begin by assuming that the spin-coating process deposits a layer of polymer of uniform height h_{dry} (e.g., the quantity s_f from equation (2)) on top of all mesas and all trenches. The main question of this section is: how does this polymer move during the annealing process? An answer to this question is needed in order to determine how much polymer eventually resides in the trenches, and how much remains on the mesas. Again, a complete model of the flow during annealing was outside the scope of the study group,

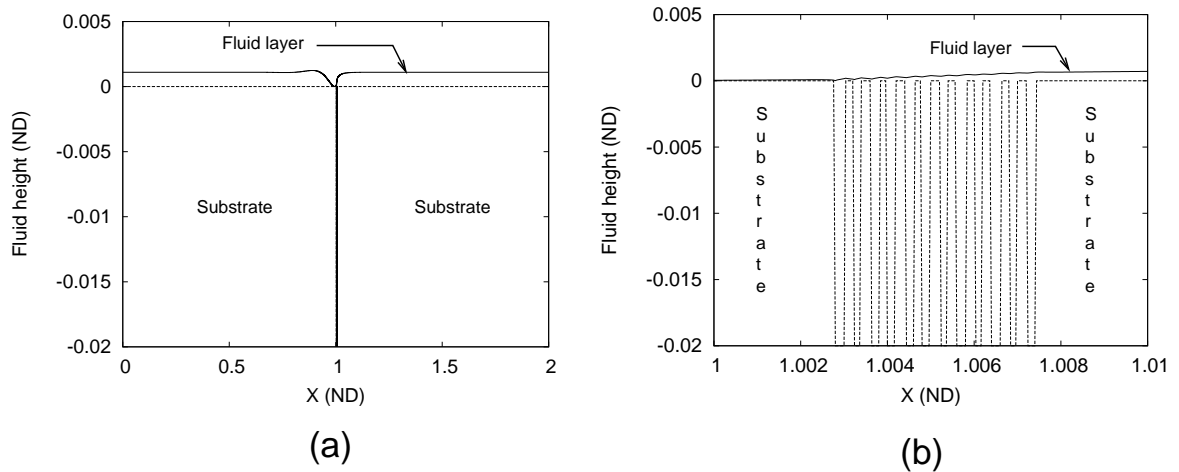


Figure 13: Final fluid layer over the set of trenches (1-2)

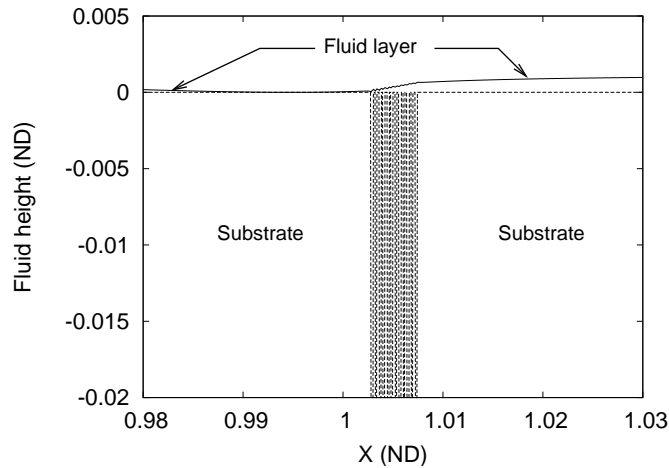


Figure 14: Final fluid layer over the set of trenches (3)

but we noted that if the annealing is sufficiently long, all models would predict that the polymer surface would become as flat as possible.

Figure 15 shows the two extreme scenarios we considered. If no flow of polymer occurs during the anneal process, then there will be a polymer depth of exactly h_{dry} everywhere, and in particular the depth in each trench is h_{dry} . On the other hand, if the molten (or glassy) polymer flows easily during the annealing, then after a sufficiently long time all polymer should be in the trenches (as in bottom part of Figure 15). Conservation of polymer mass then implies a simple relationship between the polymer in-trench depth in both cases. Now if we are looking at a high density array of trenches (periodic in one direction) with trench width w and mesa width m , then the arguments above imply a lower bound h_{low} and an upper bound

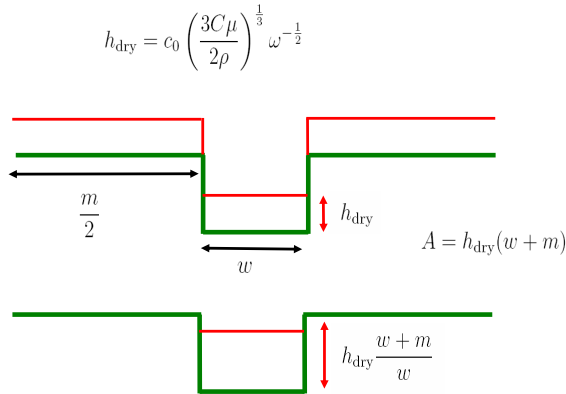


Figure 15: Limiting cases for flow under annealing. Top: no flow during anneal leaves polymer of constant depth on all mesas and in trenches: this gives a lower bound for the amount of polymer in a trench. Bottom: upper bound for depth of fill is given by the situation where all polymer from the local mesa flows into the trench.

h_{max} on the depth of polymer in each trench given by:

$$h_{\text{low}} = h_{\text{dry}}; \quad h_{\text{max}} = h_{\text{dry}} \frac{w + m}{w}, \quad (31)$$

where m is the total mesa width between each trench, and w is the trench width. Figure 16 shows a comparison of these bounds with experimentally measured polymer depths for various mesa/trench configurations [14, 15]. The theoretical bounds bracket the measured value in the majority of cases, but for several of the most-filled cases the bounds are violated. It is noteworthy that these cases correspond to the highest initial polymer concentrations, and we hypothesize that the formula used for the height h_{dry} may not be applicable here, perhaps because of nonlinear dependence of the viscosity upon concentration. If this explanation is correct, it would be most easily verified by experimentally measuring the polymer height on a flat surface to test the formula for h_{dry} : this suggested experiment (and others) are described in section 0.6 below.

0.5 Pattern formation due to self-assembly of polymers

Following a study of the existing literature on Monte-Carlo modelling of the self-assembly process, it became clear that full numerical simulation of the equations requires extensive computational resources. For the purposes of the study group, we therefore restricted our attention to two toy models which exhibit pattern-formation phenomena which bear at least some superficial resemblance to the actual complex process of diblock copolymer self-assembly. A particular focus of interest for CRANN is the problem of creating polymer patterns which can bend around corners without incurring defects. A coarse-grained model based on an extended Cahn-Hilliard approach is solved numerically in section 0.5.1, but the numerical solution breaks down when we attempt to apply to corner geometries. An independent mesoscopic Monte-Carlo model was also developed, and its results are described in section 0.5.2

Mesa width (nm)	Trench width (nm)	percent wt. (%)	Trench depth (nm)	Lower bound (nm)	Upper bound (nm)	Measured Depth (nm)
665	166	0.5	60	14.6	72.9	43
550	282	0.6	60	17.5	51.5	39
355	433	0.6	60	17.5	31.8	25
550	282	0.6	60	17.5	51.5	21
550	282	0.6	60	17.5	51.5	21
355	433	0.7	60	20.4	37.1	40 to 49
355	433	0.8	60	23.3	42.4	c 60 ?
355	433	1	60	29.1	53.0	c 100 ?

Figure 16: Table showing lower and upper bounds from equation (31) and experimentally measured values for the depth of polymer in trenches, following annealing for a time period of 1 to 3 hours. For the first five rows the theoretical bounds bracket the measured value, but the last rows show measured values outside the theoretically attainable range (in red).

0.5.1 Extended Cahn-Hilliard equation

An extension of the Cahn-Hilliard model for ordering processes in binary alloys is described and implemented in [16]. In this phenomenological approach, the concentration field $\phi(\mathbf{x}, t)$ represents the local concentration difference between the two components (here the two types of polymer). The dynamical evolution following a quench from a high-temperature disordered state is modeled by the equation

$$\frac{\partial \phi}{\partial t} = \nabla^2 (-\phi + \phi^3 - \alpha \nabla^2 \phi) - \gamma \phi. \quad (32)$$

This dimensionless form of the equation contains two parameters α and γ , and spontaneous formation of patterns may be observed when these parameters have sufficiently low values. A detailed study of this equation has not been carried out, but the qualitative behaviour is as shown in Figure 17. The three panels of this Figure show the field $\phi(\mathbf{x}, t)$ in a square geometry at (nondimensional) times $t = 0$, $t = 0.005$, and $t = 0.1$; the solution is obtained using the finite element package Comsol Multiphysics. By the last of these times the field has entered a steady-state configuration, with a characteristic stripe width. Note the x -independent initial condition $\phi(x, y, 0) = \sin(0.05y)$ was chosen as a seed for the formation of stripes oriented in the x -direction, but the steady-state stripe width is independent of the initial condition. By seeded with a y -independent initial condition it is also possible to generate stripes in the vertical direction. Interestingly, however, we were unable to find steady-state solutions for a corner geometry, where it would be desirable for a horizontally-striped solution and vertically-striped solution to merge. It is not clear at this stage whether this inability to find a steady-state corner solution is related to the experimental difficulties experienced in assembling polymer in defect-free patterns at corners.

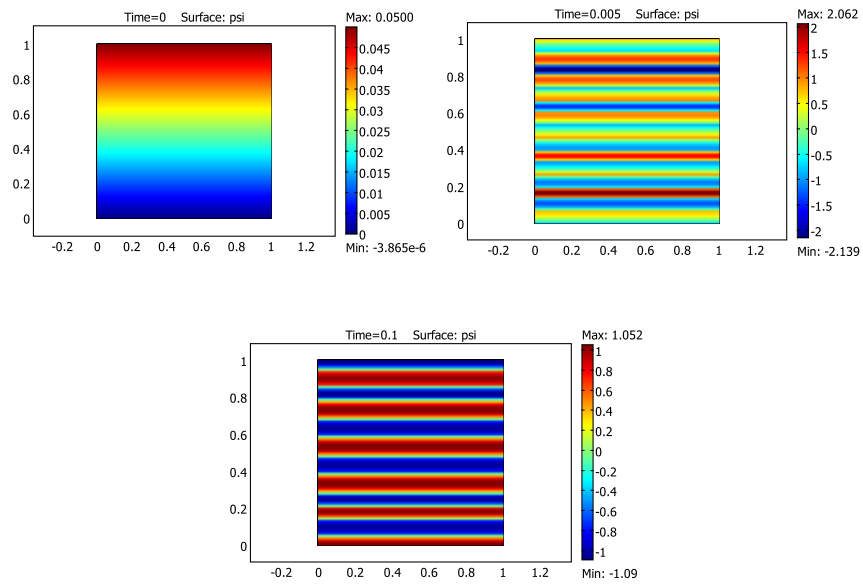


Figure 17: Snapshots of the solution field ϕ of the equation (32) in a square geometry, with parameters $\alpha = \gamma = 10^{-4}$: (a) initial condition is a small perturbation of the zero state ($\phi(x, y, 0) = \sin(0.05y)$); (b) shows the field at time $t = 0.005$; (c) steady state reached by $t = 0.1$. Note the formation of the periodic stripe structure, with a well-defined wavelength.

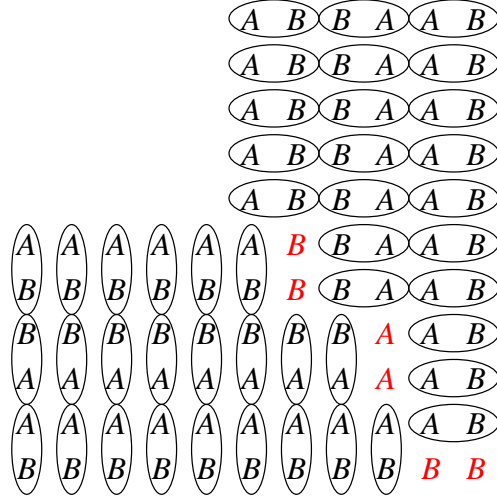


Figure 18: The local conservation of A and B blocks in a diblock copolymer microstructure makes it impossible to form a microstructure in which lamellae turn corners. The microstructure can only be accommodated by introducing isolated A and B blocks (shown in red).

0.5.2 Mesoscopic Monte Carlo Modelling

A diblock copolymer has the structure

$$\dots -a-a-a-a-b-b-b-b-b-b-\dots$$

which can be abbreviated as $A-B$ for simplicity. $-a-$ and $-b-$ are monomer groups with heterogeneous properties, for instance $-a-$ may be hydrophobic while $-b-$ is hydrophilic. While at high temperatures the two monomer chains intermingle freely, at lower temperatures an order-disorder transition occurs in which the two chains attempt to segregate. If the two blocks are of roughly equal size, the polymers segregate into lamellae. Since the A and B blocks are joined by covalent bonds the microstructure must locally conserve the ratio of A to B . This constraint does not affect straight lamellae but is violated in corner geometries as shown in Figure 18.

We use Monte Carlo simulations to investigate ordering at corner geometries and the effect of adding homogeneous polymers. Monte Carlo simulations are ideal for investigating order-disorder transitions. Since the simulations anneal the system, they can be used to explore the energy landscape. In this mesoscopic approach we treat a whole polymer block as a single entity, neglecting the internal degrees of freedom of the individual monomer units. For instance, this model does not make any distinction between the case when the polymer chains of two distinct molecules are entangled and when they are merely adjacent. To reduce computing time and to keep the simulations simple we work in two dimensions.

The Hamiltonian of the system is given by

$$H = - \sum_{\mathcal{L}_{i,j}} JS_i S_j - \sum_{\mathcal{L}_{i,\text{wall}}} JS_i \quad (33)$$

where the notation $\sum_{\mathcal{L}_{i,j}}$ means summation over nearest neighbour blocks which are part of distinct polymer chains, and $\sum_{\mathcal{L}_{i,\text{wall}}}$ means summation over cells closest to the walls. We assume that lithography has been used to coat the walls with a compound which mimics the effect of a nearby A polymer chain.

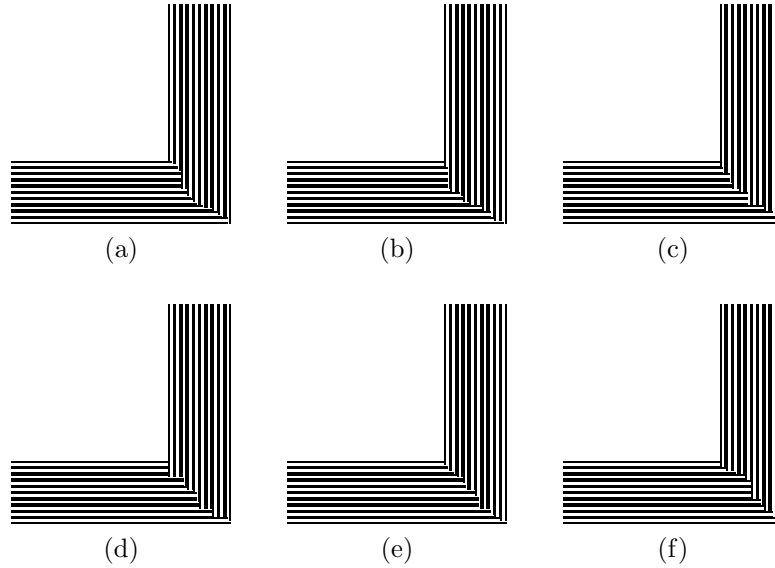


Figure 19: Degenerate ground states found for the six state system. A blocks are shown in black and B blocks in white.

In practice the algorithm breaks down the system into two by two blocks which can be in one of the six states shown below. This restriction imposes local conservation of A and B blocks.

$$\begin{bmatrix} A & B \\ A & B \end{bmatrix} \quad \begin{bmatrix} B & A \\ B & A \end{bmatrix} \quad \begin{bmatrix} A & A \\ B & B \end{bmatrix} \\ \begin{bmatrix} B & B \\ A & A \end{bmatrix} \quad \begin{bmatrix} A & B \\ B & A \end{bmatrix} \quad \begin{bmatrix} B & A \\ A & B \end{bmatrix}$$

Annealing this system finds a degenerate ground state with ordered lamellae leading into the corner but without a unique ordered state at the corner. This behaviour is characteristic of geometrically frustrated systems in which it is impossible to satisfy all the interactions of a system due to geometrical constraints [17, 18, 19]. Examples of degenerate ground states found by the simulation are shown in Figure 19.

The degeneracy can be broken by allowing the inclusion of homogeneous polymers. If the states

$$\begin{bmatrix} A & B \\ B & B \end{bmatrix} \quad \begin{bmatrix} B & A \\ A & A \end{bmatrix}$$

are included then the simulation finds a unique ordered ground state in which the lamellae persist around the corner. This ground state is shown in Figure 20.

0.6 Conclusions and further work

To summarize: this report details work on several aspects of the complex modelling problem presented by CRANN researchers. In section 0.2 we have included a review of modelling work for spin-coating onto flat substrate, including some recent progress on improving Meyerhofer's solution method. Section 0.3 documents our work on developing a model for the flow of the solvent (with dilute solute) over a non-flat topography, and includes analytical and numerical solutions for flow over trenches. To provide a (partial)

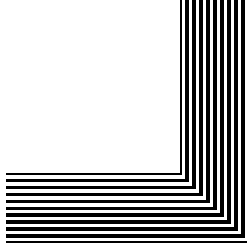


Figure 20: Unique ground state found for the eight state model.

answer to CRANN’s query regarding optimizing mesa/trench configurations in high-density arrays, we use a simple mass-balance argument in section 0.4 to obtain bounds on the in-trench polymer height—these appear to agree quite well with the available experimental data. Exceptions arise at higher concentrations of polymer, which possibly indicates a strong effect of the concentration-dependent viscosity in these cases. Finally, in section 0.5 we review our work on models of pattern formation for the self-assembly process—though very phenomenological, it is possible that further work on one or both of the models suggested could lead to useful insights.

An important part of the modelling process involves suggesting experiments which would provide useful information or feedback to the models. With this in mind, we propose the following experiments:

1. Spin-coat onto a flat surface and measure the dry film thickness. This will validate the model of section 0.2, and permit calibration of parameters appearing in the Meyerhofer formula.
2. If these experimental results do not match the predictions (especially at higher concentrations of polymer), it will be necessary to include the concentration-dependence of viscosity in our equations. Measurement of the viscosity of the solutions used at various concentrations would therefore be very useful.
3. Measure the profile of polymer following flow over topography (but before annealing) and compare with the predictions in section 0.3.
4. Measure the profile of the polymer (on topography) after annealing for various times. Results of these experiments are required to extend the modelling of section 0.4 beyond the rather simplistic steady-state assumptions used here.

Nomenclature

c	Solute concentration	0-1	ND
g	Gravity	9.8	$\text{m}\cdot\text{s}^{-2}$
h	Fluid height		ND
p	Pressure		ND
s	Solute height		ND
t	Time		ND
$\vec{u} = (u, v, w)$	Velocity vector		ND
(x, y, z)	Cartesian coordinates		ND
E	Evaporation velocity	$2.5833 \cdot 10^{-6}$	$\text{m}\cdot\text{s}^{-1}$
$\mathbf{Q} = (Q^x, Q^y)$	Cartesian flux		ND
U	Velocity scale		$\text{m}\cdot\text{s}^{-1}$
α	$\epsilon\sigma/(\rho\omega^2L^3)$		ND
β	$\epsilon g/(L\omega^2)$		ND
δ	Surface topography to fluid thickness ratio		ND
$\epsilon = H/L$	Aspect ratio	0.0025	ND
μ	Dynamic viscosity	$62 \cdot 10^{-5}$	$\text{kg}\cdot\text{m}^{-1}\cdot\text{s}^{-1}$
ρ	Fluid density	867	$\text{kg}\cdot\text{m}^{-3}$
σ	Surface tension	$28.4 \cdot 10^{-3}$	$\text{kg}\cdot\text{s}^{-2}$
ω	Angular velocity	335	$\text{rad}\cdot\text{s}^{-1}$

.1 General solution of Equation (17) using the Green function

The leading order solution of Equation (17) only depends on time and may be approximated as:

$$\frac{dh_0}{dt} = -2h_0^3 - 1. \quad (34)$$

The corresponding first order film height equation is:

$$6(h_1 + s_1) + 3 \left[x \frac{\partial(h_1 + s_1)}{\partial x} + y \frac{\partial(h_1 + s_1)}{\partial y} \right] + \alpha h_0 \left[\frac{\partial^4 h_1}{\partial x^4} + 2 \frac{\partial^4 h_1}{\partial x^2 \partial y^2} + \frac{\partial^4 h_1}{\partial y^4} \right] - \beta h_0 \left[\frac{\partial^2 h_1}{\partial x^2} + \frac{\partial^2 h_1}{\partial y^2} \right] = 0. \quad (35)$$

The first order film height may be solved using the Green function, $G(x - x_0, y - y_0)$, defined as the solution of equation and the function $f(x, y)$:

$$6G + 3 \left[x \frac{\partial G}{\partial x} + y \frac{\partial G}{\partial y} \right] + \alpha h_0 \left[\frac{\partial^4 G}{\partial x^4} + 2 \frac{\partial^4 G}{\partial x^2 \partial y^2} + \frac{\partial^4 G}{\partial y^4} \right] - \beta h_0 \left[\frac{\partial^2 G}{\partial x^2} + \frac{\partial^2 G}{\partial y^2} \right] = \delta(x - x_0)\delta(y - y_0), \quad (36)$$

where $\delta(x - x_0)\delta(y - y_0)$ is the Dirac Delta function in R^2 and the function $f(x, y)$ is defined as:

$$f(x, y) = -3 \left[x \frac{\partial s_1}{\partial x} + y \frac{\partial s_1}{\partial y} \right] - 6s_1. \quad (37)$$

Applying the transform

$$\bar{G}(v, y) = \int_{-\infty}^{\infty} \exp(-ivx)G(x, y)dx, \quad (38)$$

to Equation (35), we obtain

$$\alpha h_0 \left[v^4 \bar{G} - 2v^2 \frac{d^2 \bar{G}}{dy^2} + \frac{d^4 \bar{G}}{dy^4} \right] - \beta h_0 \left[-v^2 \bar{G} + \frac{d^2 \bar{G}}{dy^2} \right] + 6\bar{G} + 3 \left[\frac{\bar{G}}{iv - 1} + y \frac{d\bar{G}}{dy} \right] = \delta(y - y_0)e^{-ivx_0}. \quad (39)$$

Applying the transform

$$\tilde{G}(v, w) = \int_{-\infty}^{\infty} \exp(-iwy) \bar{G}(v, y) dy, \quad (40)$$

to (39), we obtain

$$\alpha h_0 \left[v^4 \tilde{G} + 2v^2 w^2 \tilde{G} + w^4 \tilde{G} \right] - \beta h_0 \left[-v^2 \tilde{G} - w^2 \tilde{G} \right] + 6\tilde{G} - 3 \left[\frac{\tilde{G}}{iv-1} + \frac{\tilde{G}}{iw-1} \right] = \exp[-i(vx_0 + wy_0)]. \quad (41)$$

Rearranging (41), we find

$$\tilde{G} = \frac{\exp[-i(vx_0 + wy_0)]}{h_0(v^2 + w^2) [\alpha(v^2 + w^2) + \beta] + 6 - 3 \left[\frac{1+iv}{1+v^2} + \frac{1+iw}{1+w^2} \right]}. \quad (42)$$

Applying two inverse transforms to (42), we get an expression for G , as follows

$$G(x - x_0, y - y_0) = \frac{1}{4\pi^2} \int_{-\infty}^{\infty} \int_{-\infty}^{\infty} \frac{\exp[i(v(x - x_0) + w(y - y_0))] dv dw}{h_0(v^2 + w^2) [\alpha(v^2 + w^2) + \beta] + 6 - 3 \left[\frac{1+iv}{1+v^2} + \frac{1+iw}{1+w^2} \right]}. \quad (43)$$

The first order perturbation, h_1 , may then be calculated using the function $f(x, y)$:

$$h_1(x, y) = \int_{-\infty}^{\infty} \int_{-\infty}^{\infty} f(x_0, y_0) G(x - x_0, y - y_0) dx_0 dy_0, \quad (44)$$

where $f(x, y)$ and $G(x - x_0, y - y_0)$ are given by (37) and (43) respectively.

Bibliography

- [1] Section IV of A.K. Chakraborty and A.J. Golombfskie. *Annual Review of Physical Chemistry*, 52:537 (2001).
- [2] A.G. Emslie, F.T. Bonner and L.G. Peck. Flow of a viscous liquid on a rotating disk. *Journal of Physics*, 29(5):858–862, 1998.
- [3] D. Meyerhofer. Characteristics of resist films produced by spinning. *Journal of Physics*, 49(7):3993–3997, 1978.
- [4] V.Cregan and S.B.G. O’Brien. A note on spin-coating with small evaporation. *Journal of Colloid and Interface Science*, 314(1):324–328, 2007.
- [5] H. Ockendon and J.R. Ockendon. *Viscous Flow*. CUP, 1995.
- [6] A. Oron, S.H. Davis and S.G. Bankhoff. Long scale evolution of thin liquid films. *Reviews of Modern Physics*, 69(3):931–980, 1997.
- [7] P.H. Gaskell, P.K. Jimack, M. Sellier, H.M. Thompson and C.T. Wilson. Gravity-driven flow of continuous thin liquid films on non-porous substrates with topography. *Journal of Fluid Mechanics*, 509:253–280, 2004.
- [8] S. Kalliadasis and C. Bielarz. Steady free-surface thin film flows over topography. *Physics of Fluids*, 12(8):1889–1898, 2000.
- [9] L.M. Peurrung and D.B. Graves. Film thickness profiles over topography in spin coating. *Journal of the Electrochemical Society*, 138(7):2115–2124, 1991.
- [10] J.P.F. Charpin and T.G. Myers. Modelling thin film flows with erosion and deposition. *Advances in Water Resources*, 28:761–772, 2005.
- [11] J.A. Moriarty and L.W. Schwartz. Unsteady spreading of thin liquid films with small surface tension. *Physics of Fluids*, A3(5):733–742, 1991.
- [12] N.N. Yanenko. *The method of fractional steps*. Springer, 1971.
- [13] J.W. Thomas. *Numerical Partial Differential Equations: Finite Difference Methods*. Texts in Applied Mathematics (22). Springer, 1995.
- [14] T.G. Fitzgerald, F. Borsetto, J.M. O’Callaghan, B. Kosmala, J.D. Holmes, and M.A. Morris. Polymer nanostructures in sub-micron lithographically defined channels: film-thickness effects on structural alignment of small feature size polystyrene-polyisoprene-polystyrene block copolymer *Soft Matter*, 3:916–921 (2007)

- [15] T.G. Fitzgerald, personal communication.
- [16] H. Chen and A. Chakrabarti. Morphology of thin block copolymer films on chemically patterned substrates. *J. Chem. Phys.* 108:6897905 (1998).
- [17] A.P. Ramirez, G.P. Espinosa and A. S. Cooper. Strong frustration and dilution-enhanced order in a quasi-2D spin glass. *Phys. Rev. Lett.* 64:2070–3 (1990).
- [18] A.P. Ramirez. Strongly geometrically frustrated magnets. *Annu. Rev. Mater. Sci.* 24:453–480 (1994).
- [19] A.P. Ramirez. Geometric frustration: magic moments. *Nature* , 421:483 (2003).